Enabling Rapid Charging Lithium Metal Batteries via Surface Acoustic Wave-Driven Electrolyte Flow

An Huang, Haodong Liu, Ofer Manor, Ping Liu, and James Friend*

Both powerful and unstable, practical lithium metal batteries have remained a difficult challenge for over 50 years. With severe ion depletion gradients in the electrolyte during charging, they rapidly develop porosity, dendrites, and dead Li that cause poor performance and, all too often, spectacular failure. Remarkably, incorporating a small, 100 MHz surface acoustic wave device (SAW) solves this problem. Providing acoustic streaming electrolyte flow during charging, the device enables dense Li plating and avoids porosity and dendrites. SAW-integrated Li cells can operate up to 6 mA cm^{-2} in a commercial carbonate-based electrolyte; omitting the SAW leads to short circuiting at 2 mA cm^{-2}. The Li deposition is morphologically dendrite-free and close to theoretical density when cycling with the SAW. With a 245 µm thick Li anode in a full Li∥LFP (LiFePO$_4$) cell, introducing the SAW increases the uncycled Li from 145 to 225 µm, decreasing Li consumption from 41% to only 8%. A closed-form model is provided to explain the phenomena and serve as a design tool for integrating this chemistry-agnostic approach into batteries whatever the chemistry within.

The rechargeable battery is the key to improving a broad swath of technology for society, from consumer and defense electronics, grid energy storage, and robotics to electric vehicles for sustainable transport.[1,2] Safety, rechargeability, specific capacity, and lifetime still need improvement: the best lithium-ion battery today (240 Wh kg^{-1}) offers only six times the energy density of a lead–acid battery (40 Wh kg^{-1}) from 120 years ago.[3–5] As current state of the art Li-ion batteries (LIBs) approach their theoretical limits by using lithiated graphite and meticulously engineered electrolytes, alternatives are sought

to increase the energy density in batteries for emerging electronic devices.[6] Lithium metal (Li) is the ideal choice as an anode in Li metal batteries (LMBs) with a potential to deliver an energy density of 500 Wh kg^{-1}, at least double today's best LIB.[1] The decision in the 1980s to abandon LMBs after years of research and adopt LIBs was in recognition of the difficult problem of dendrites forming on the Li metal anode during recharging. The dendrites will not only penetrate the separator and lead to serious safety issues but also will lead to low Coloumbic efficiency and a substantial reduction in charge capacity as they consume both Li and electrolyte.[7] These issues have long impeded commercialization of Li metal batteries (LMB) despite their otherwise overwhelming advantages.[8,9]

Beyond chemistry, external magnetic forces have also been proposed to inhibit continuous growth of the dendrite tips through magnetohydrodynamics.[10,11] However, the energy consumption is high and the performance is limited. Ultrasound has been used to drive acoustic streaming-driven fluid stirring and enhance the uniformity of ion distribution during traditional chemical vapor deposition.[12,13] However, the ultrasonicators in these past works have always been large, inefficient, electrochemically incompatible, and very heavy—unsuitable for integration into a practical LMB. By contrast, surface acoustic wave (SAW) devices offer extraordinary power density in a fingernail-sized device, and are useful in drop handling, biological sensors, cell manipulation, and particle collection in microfluidics.[14–17] Uniquely, they generate locally extreme accelerations of 10^8–10^{10} m s^{-2}, driving acoustic streaming-driven fluid flow at up to 1 m s^{-1}, and imparting acoustic forces upon objects present in the fluid, such as cells and micro to nanoscale particles.[18] SAW devices can be inexpensively produced through a standard ultraviolet photolithography and lift-off process to deposit interdigitated metallic electrodes onto a low-loss, single crystal piezoelectric Li niobate substrate, a commodity from decades of development and use in telecommunications.[19]

In this work, we expect to overcome the two underlying problems hampering rechargeable battery progress for over 50 years: protracted charging times and inadequate lifetime due to unfavorable morphological changes. We especially seek to avoid Li dendrites when metal deposition processes are employed in a carbonate-based electrolyte, EC/DEC, which is notorious[20] for Li dendrite formation and caused by ion depletion in the

A. Huang, Prof. J. Friend
Materials Science and Engineering Program and
the Department of Mechanical and Aerospace Engineering
University of California San Diego
9500 Gilman Drive, La Jolla, CA 92093, USA
E-mail: jfriend@eng.ucsd.edu
Dr. H. Liu, Prof. P. Liu
Materials Science and Engineering Program
and the Department of Nanoengineering
University of California San Diego
9500 Gilman Drive, La Jolla, CA 92093, USA
Prof. O. Manor
Wolfson Department of Chemical Engineering
Technion—Israel Institute of Technology
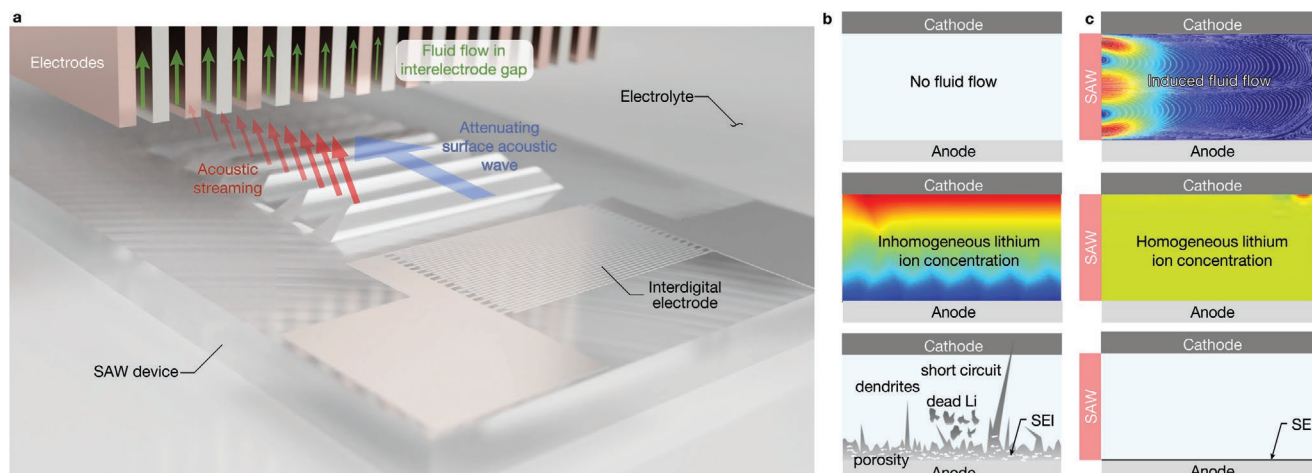Haifa 3200003, Israel

1907516 (1 of 7)

Figure 1. A comparison of the working principles of traditional and SAW-driven Li metal batteries. a) Illustration of how acoustic streaming drives electrolyte flow in the gap(s) between the electrode(s). b,c) A traditional LMB (b) compared to a SAW LMB (c) based upon computations of the flow and ion distribution. For a traditional LMB, the stationary electrolyte permits high ion concentration gradients to appear during charging, producing Li dendrite formation, dead Li, Li metal volume expansion, uneven solid electrolyte interface (SEI) formation, and, eventually, short circuit of the cell. By contrast, in a SAW LMB, acoustic streaming recirculates the electrolyte, leading to a homogeneous ion distribution and uniform Li deposition during charging.

electrolyte adjacent the anode. A SAW-integrated LMB (SAW LMB) is therefore proposed, as shown in **Figure 1**, as a new route to potentially overcome these longstanding problems. By driving sufficient flow of the electrolyte through the interelectrode gap, it becomes possible to prevent the formation of Li ion depletion regions, thus preventing dendrites, adverse heating, and electrolyte breakdown. The flow is driven by acoustic (fluid) streaming generated by the SAW device, significantly reducing the Li concentration gradient in the electrolyte—even during rapid charging—and uniform Li deposition is made possible. The power consumption of the SAW device is around 10 mWh cm^{-2}, relatively small in comparison to the charging itself, and in any case occurring when power consumption is acceptable: during charging. During LMB discharge, dendrites do not form, and so the SAW device may remain off. In what follows, we report the results of galvanostatic cycling and post cycling analysis of prototype Li metal batteries to describe the beneficial effects of using SAW in them. Furthermore, we provide a closed-form model that both describes the underpinning physics and can be used to design the SAW device for a given battery configuration.

We first consider the Li deposition morphology on a copper (Cu) substrate using a carbonate based electrolyte of 1 M LiPF$_6$ in ethylene carbonate/dietheryl carbonate (EC/DEC; Figure S3, Supporting Information). The carbonate electrolyte was chosen as our baseline electrolyte because it is known to be compatible with 4 V cathode materials and is capable of triggering dendrite formation at current densities of only 0.5 mA cm^{-2} in an Li anode cell.[21,22] The Li was electrochemically plated onto the Cu substrate at a current density of 1 mA cm^{-2} (1 C) until the areal capacity reached 1 mAh cm^{-2} for both baseline and SAW Li‖Cu cells (the deposition profile is shown in Figure S3a in the Supporting Information). The voltage of the baseline cell continued to decrease as Li was deposited, while the SAW cell exhibited a constant voltage near −0.1 V, indicating stable electrodeposition and perhaps homogeneous deposition.[23] Upon increasing the deposition current density to 6 mA cm^{-2} (6 C) for cells with and

without SAW (Figure S3b, Supporting Information), similar trends were observed. A more drastic drop in the deposition voltage was observed in the early stage of the deposition for the baseline cell, followed by a continued drop from −0.3 V at 0.1 mAh to −0.58 V at 1 mAh. In contrast, the SAW Li‖Cu cell showed a nearly identical voltage profile, becoming constant at −0.1 V. Notably, the baseline cell exhibited a deep voltage drop at the beginning of the 6 mA cm^{-2} deposition (circled in Figure S3b in the Supporting Information). This phenomenon has been seen before and is associated with the overpotential due to a heterogeneous nucleation barrier from the thermodynamic mismatch between Li and Cu,[24] and appears to be absent when using SAW.

The cycled cells were then disassembled and the electrodes were collected for scanning electron microscopy (SEM). When cycled at 1 mA cm^{-2} current density, the presence of SAW reduces the thickness of the deposited Li from 9.1 µm without SAW in the baseline cell to 5.3 µm with SAW. The thickness of the deposition is an indication of its density. A 4.85 µm thickness may theoretically be achieved if the deposition is completely dense without porosity or dendrites.[25] While the SEI is a factor, its volume is insignificant compared to the dead Li present in the battery based on recent published data.[26] Based on these values, the porosities of the deposited Li are 46.7% and 8.5% for the baseline cell and SAW cell, respectively. The Li‖Cu cell produces better deposition behavior with SAW than without it. The top view images further support this conclusion, as the deposition morphology is dense and without dendrites for the SAW Li‖Cu cell (**Figure 2**g,h) while porosity and dendrites are present in the baseline Li‖Cu cell (Figure 2c,d).

We further examined the Li‖Cu cells' electrodes after Li deposition at a current density of 6 mA cm^{-2}. The Li deposition thickness in the baseline cell increased threefold from 9.1 to 27 µm, giving an extremely high porosity of 82%, an indication of dendrite formation and loose deposition.[27] By comparison, the deposition thickness is far less when using SAW, 6 µm, with a much lower porosity of 19%. Though the porosity is certainly

ADVANCED
SCIENCE NEWS
www.advancedsciencenews.com

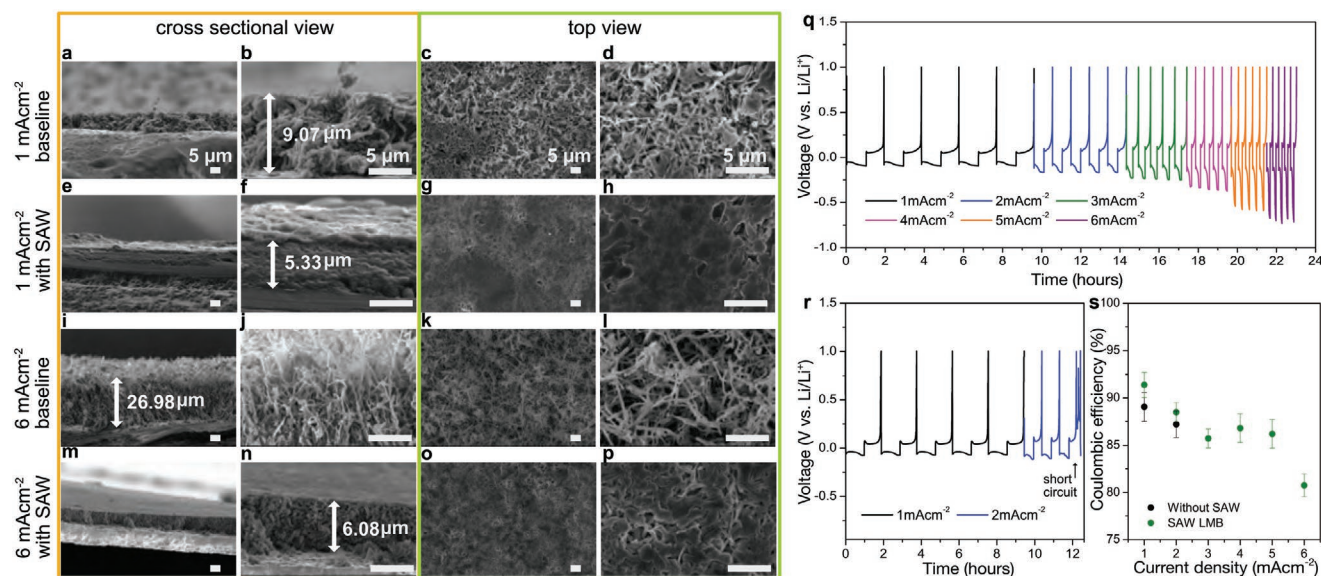ADVANCED
MATERIALS
www.advmat.de

Figure 2. SEM images of the Cu electrodes in the Li‖Cu system with and without SAW after the first deposition cycle. Images of the Cu electrode after plating 1 mAh cm⁻² areal capacity of Li under 1 mA cm⁻². a–d) The baseline Li‖Cu system shows substantially different morphology than e–h) with SAW under the same conditions. Images of the Cu electrode after plating 1 mAh cm⁻² areal capacity under 6 mA cm⁻². i–l) Baseline and m–p) SAW-driven Li‖Cu cell. Note the views among each column are at the same scale, with cross-sections a,b,e,f,i,j,m,n) and top views (c,d,g,h,k,l,o,p) of the Cu electrode. Moreover, the comparison of Coulombic efficiency of Li‖Cu batteries with and without SAW at various deposition and stripping rates. The testing current densities incrementally progressed from 1 mA cm⁻² to 2, 3, 4, 5, and 6 mA cm⁻² until—in each case—the deposition reached areal capacity of 1 mAh cm⁻² and was stripped back to 1 V, producing an electrochemical profile of the Li‖Cu cell with SAW (q) and without SAW (r). s) The average Coloumbic efficiency of the baseline (black dots) and SAW-driven Li‖Cu (green dots) are shown as a function of the current density.

higher at 6 than at 1 mA cm⁻², using SAW produces far better deposition behavior. Again, the top view images support this conclusion, with substantial porosity and dendrites in the cell without SAW (Figure 2k,l) and homogeneous "chunked" morphology with SAW (Figure 2p) known to result from homogeneous current distribution during deposition.[28]

Moreover, we investigated the deposition morphology of Li on Cu after charging to 1 mAh cm⁻² charge capacity at a current density of 6 mA cm⁻² while using SAW input powers of 40 and 500 mW, less and greater, respectively, than the 100 mW used in Figure 2. At low SAW input power (40 mW), the thickness of Li at 6 mAh cm⁻² is 8.75 µm (Figure S4a,b, Supporting Information). The deposition thickness is greater than the 6.08 µm deposition thickness obtained at a SAW power of 100 mW (Figure 2n). However, it is much thinner than the 27 µm of Li deposited in the baseline cell (Figure 2i). Moreover, viewed from the top, the Li morphology is a mixture of dendrites and chunks (Figure S4c,d, Supporting Information), indicating that when an insufficient power is applied, the effect of acoustic streaming on the Li⁺ concentration gradient is limited, resulting in a less dense Li deposition. However, increasing the SAW input power to 500 mW produces a 7.5 µm thick layer of Li (Figure S4e,f, Supporting Information), between the deposition thicknesses found when using 40 mW (8.75 µm) and 100 mW (6.08 µm). The deposition morphology at 500 mW SAW power is a chunk-like structure (Figure S4g,h, Supporting Information).

We also examined the Coulombic efficiency of the Li‖Cu cell with the same carbonate electrolyte at different current densities, both with and without SAW (Figure 2q,r). At 1 and 2 mA cm⁻², the average Coulombic efficiencies are 91.5% and

89% with SAW, nearly identical to the baseline cell without SAW, at 88% and 87%, respectively. However, at 2 mA cm⁻² the baseline cell exhibits signs of a short circuit with an unstable electrochemistry profile in the third cycle. By contrast, the SAW Li‖Cu cell continues to show good cycling performance even to the extremely high cycling rate of 6 mA cm⁻², maintaining 80% Coloumbic efficiency throughout.

We assembled a full Li‖LiFePO₄ (Li‖LFP) cell to investigate the practical aspects of integrating a SAW device into a battery, using LFP as the cathode with an areal capacity of 1 mAh cm⁻². The effect of SAW on the high charge rate capability of Li‖LFP cells is illustrated in **Figure 3** using 1M LiPF₆ in EC/DEC carbonate electrolyte at different current densities. Both charge and discharge are conducted at the same current density for this test. At a low current density of 0.5 mA cm⁻²(0.5 C), both the baseline Li‖LFP cell and SAW Li‖LFP cell exhibit a discharge capacity of about 137 mAh/g, due to the small Li⁺ concentration gradient present in the electrolyte at this current density, whether or not SAW is circulating the electrolyte. As the current density increases beyond 1 mA cm⁻² (1 C), however, a visible difference appears in the charge/discharge capacity due to the SAW. At 1 mA cm⁻², the capacity is 120 mAh g⁻¹ without SAW, and 130 mAh g⁻¹ with SAW. Notably, 1 mA cm⁻² is reported as the critical current density that, upon exceeding, dendrites start to grow and the limitations of Li⁺ ion diffusion begins to impact the battery's cycling performance.[4]

As the current density is further increased to 6 mA cm⁻² (6 C), the discrepancy in capacity likewise grows due to the SAW. The baseline cell delivered only 11 mAh g⁻¹, retaining only 8% of its low-rate capacity, but using SAW in the cell provides a discharge capacity of 55 mAh g⁻¹, retaining 40%

**ADVANCED
SCIENCE NEWS**
www.advancedsciencenews.com

**ADVANCED
MATERIALS**
www.advmat.de
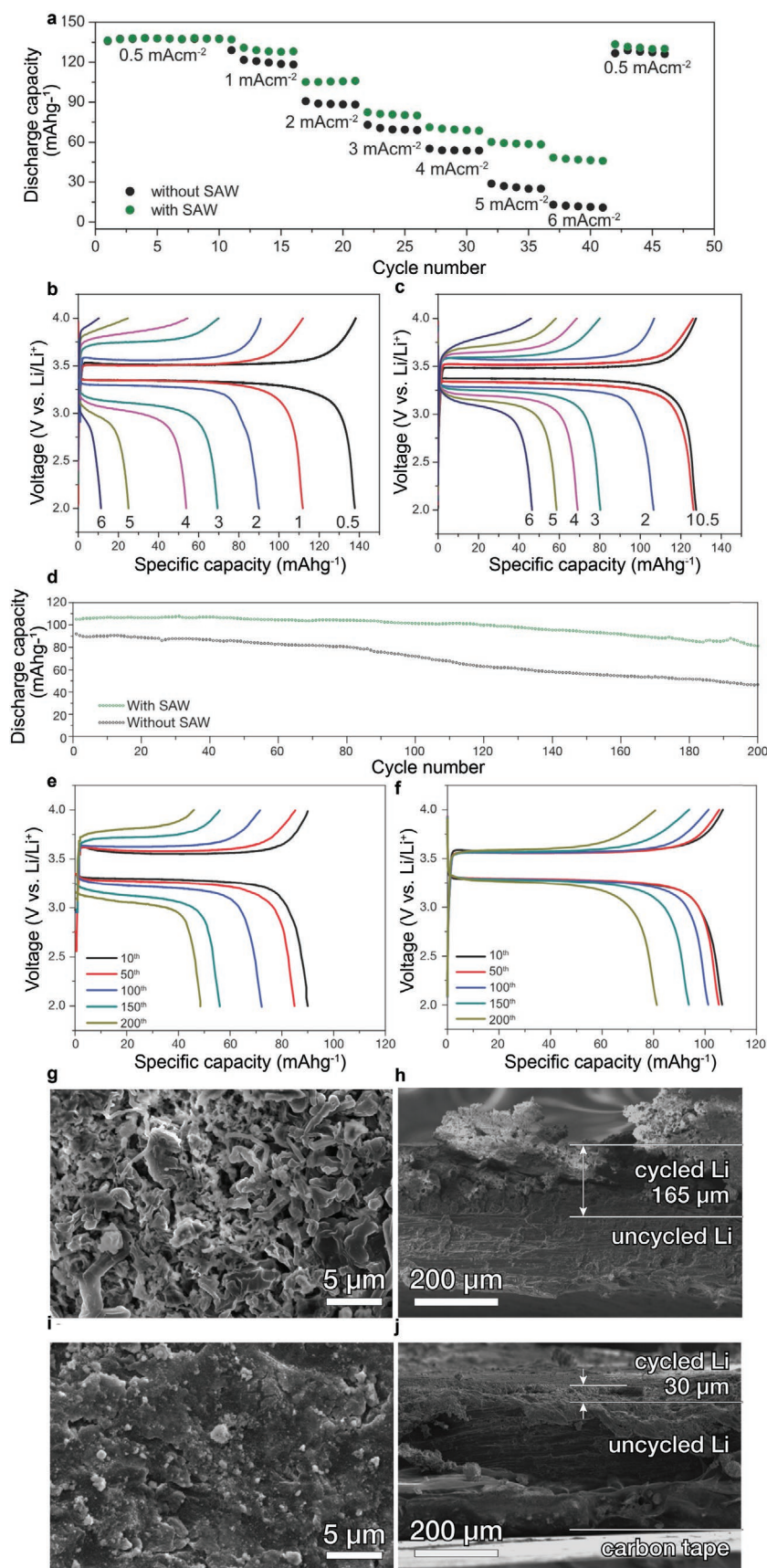
of its low-rate capacity. The SAW provides a five-fold increase in discharge capacity at 6 mA cm^{-2} (6 C). Finally, each cell was returned to the starting current density of 0.5 mA cm^{-2} (0.5 C), and the capacity was found to recover—indicating an absence of battery damage from the fast charge and discharge cycling. The SAW Li∥LFP generated a slightly higher capacity than the baseline Li∥LFP. Altogether, the drop in capacity at 6 mA cm^{-2} (6 C) is mainly due to the limited Li$^+$ ion diffusion rate, producing a corresponding large Li ion concentration gradient. Without SAW, it is not possible to charge the Li∥LFP at high current densities. But with SAW, the discharge capacity is improved despite the high current density, perhaps due to improvement of the Li$^+$ ion diffusion and reduction of the associated ion concentration gradient via SAW-driven electrolyte recirculation.

The limitations in Li$^+$ diffusion can be shown in the charge and discharge profiles of the baseline Li∥LFP (Figure 3b) and SAW Li∥LFP (Figure 3c). At high cycle rates, the voltage hysteresis dramatically increased in the baseline Li∥LFP cell to 1.02 V at 6 mA cm^{-2} (6 C) current density, 70% larger than the SAW Li∥LFP (0.59 V). The large voltage hysteresis is again an indication of the poor Li ion transportation in the baseline cell. Since the initial voltage hysteresis is similar for the cell with or without SAW, the resistance otherwise present in the cell is likewise similar.

The long term cycling stability of the SAW Li∥LFP cells was investigated by applying a

Figure 3. Electrochemical properties of baseline and SAW-driven Li∥LiFePO$_4$ cells at different cycle rates and long term cycleability. a) The discharge capacities of the baseline (black) and SAW-driven (green) Li∥LiFePO$_4$ cells are plotted versus the charge/discharge cycle at progressively greater current densities of 0.5, 1, 2, 3, 4, 5, and 6 mA cm^{-2} (1 mA cm^{-2} corresponds to 1 C). b,c) The representative charge and discharge voltage profiles of Li∥LiFePO$_4$ cells are likewise shown for current densities of 0.5, 1, 2, 3, 4, 5, and 6 mA cm^{-2} in the baseline (b) and SAW (c) Li∥LiFePO$_4$ cells. d) The discharge capacity of an Li∥LFP with (green) or without (black) SAW over 200 cycles at a current density of 2 mA cm^{-2}. e,f) The associated charge and discharge profiles of the baseline (e) and SAW (f) Li∥LFP cells are plotted at cycles 10, 50, 100, 150, and 200. g–j) Scanning electron microscopy of the morphology of Li in the Li∥LFP cell after 200 cycles. Extensive porosity and dendrites are present in a top view (g) and cross sectional view (h) of the Li anode from the SAW-absent Li∥LFP baseline cell, unlike the comparatively dense and smooth morphology of the Li anode from the SAW Li∥LFP cell (i, top view and j, cross sectional view).

current density of 2 mA cm^{-2} (2 C) for both charge and discharge over 200 cycles to Li‖LFP cells, using cut-off voltages of 2–4 V. The discharge capacity plotted in Figure 3d–f indicates superior cycle performance with SAW in the Li‖LFP cell, with a greater discharge capacity throughout, from the initial to the 200th cycle. With SAW, the Li‖LFP offers 110 mAh g^{-1} of discharge capacity, modestly more than the 90 mAh g^{-1} of the baseline Li‖LFP without SAW. After 200 cycles, however, the SAW Li‖LFP cell retained 82% of its initial discharge capacity after 200 cycles, far more than the 51% capacity retained by the baseline Li‖LFP cell.

The effect of SAW is further apparent in a comparison between the individual charge and discharge voltage profiles of the baseline Li‖LFP in Figure 3e and the SAW Li‖LFP cell in Figure 3f. The baseline cell's polarization increases with the number of cycles, and there is a 63% increase in the polarization voltage from the 10th cycle (0.28 V) to the 200th cycle (0.77 V). The increase in polarization is an indication of dead Li and Li dendrite formation,[27] leading to a reduction in discharge capacity as cycles accumulate. However, with SAW, the polarization voltage increases less than 10% from 0.266 V at the 10th cycle to 0.298 V at the 200th cycle, indicating the achievement of stable cycle performance using SAW.

The cycled Li‖LFP cells were disassembled to examine the morphology of the Li anodes using SEM (Figure 3g–j). The Li anode from the baseline cell exhibits porous morphology and dendritic growth in Figure 3g,h. However, with SAW, the Li anode morphology is comparatively dense and smooth in Figure 3i,j. Noting the total thickness of the pristine Li is 245 µm, this substantial difference may be quantified by measuring the thickness[29] of the (porous) cycled Li and (dense) uncycled Li using Figure 3i,j. The thickness of the uncycled Li is 145 µm without SAW, and is 225 µm with SAW. In the baseline Li‖LFP cell without SAW, 41% of the Li participates in the cycling. The thickness of the cycled Li increased from 100 to 165 µm after 200 cycles without SAW, a 65% increase. By contrast, with SAW in the Li‖LFP cell, only 8% of the Li is cycled, and the cycled Li increased from 20 to 30 µm after 200 cycles, a 33% increase.

The diffusion of Li$^+$ ions is crucial to the performance of Li batteries: its charge and discharge rate,[30,31] capacity, and stability. Most batteries have quiescent electrolyte, with $u = 0$ for the electrolyte velocity, leaving diffusion to migrate Li$^+$ ions across concentration gradients in the electrolyte and to the anode during charging (Figure 1b).[32] Diffusion is inadequate in high-speed charging, and by generating flow in the electrolyte, SAW-driven acoustic streaming augments diffusion—in fact supplants it—in transport of Li$^+$ ions (Figure 1c), but the details require careful analysis summarized here and provided in more detail in the Supporting Information.[33]

Past analyses typically employ spatially 1D models,[32,34] as the full problem is not easy to solve, even with a computer.[35] Here, we seek an immediately useful, closed-form result to both explain the physical phenomena and provide a tool for battery design incorporating SAW-driven electrolyte recirculation, examining how flow inhibits the early growth of small dendrites, as suggested by classic experimental work on impinging flow.[36]

We assume the cell is near its limiting current density, the worst case scenario for dendrite formation. We further assume that slight, sinusoidal morphological imperfections are present along the electrode—of wavelength λ and amplitude ϵ from the initial construction of the battery (see Figure S6 in the Supporting Information)—forming "hotspots" that locally enhance the rate by which metal ions adsorb onto the electrode and allow for the initial growth of dendrites. With our electrolyte, the Reynolds number is Re $= \rho u L/\mu \approx 0.2$–2, as a function of the density ρ, viscosity μ, and length scale L, indicating laminar, almost viscous, flow as one might expect from the dimensions of the structure, though the Li$^+$ ion convection is strong, potentially with an ion transport boundary layer of $\ell \approx 0.1$–1 µm thickness, as the diffusion coefficient[37] is $\approx 10^{-9}$ m^2 s^{-1}, due to the requirement that the leading order convective and diffusive components in the transport equations must become comparable in magnitude within the boundary layer, in turn satisfied by requiring that the corresponding Peclet number in the boundary layer is Pe $= u_c \ell/D \approx 1$ in a simplified analysis assuming the electrolyte flows as a simple shear flow with characteristic velocity u_c. The small thickness of the boundary layer compared to the interelectrode gap, and the lack of excess pressure therein supports—at least locally—our simple shear flow assumption. It is similar to a past successful approximation[38] of a parabolic velocity profile between flat and parallel electrodes as simple shear flow in the boundary layer near the electrodes.

By modeling the advective and diffusive transport of ions, both transverse and parallel to an electrode in the cell, as a 2D convection-diffusion model as detailed in the Supporting Information, we connect the acoustically driven electrolyte flow in the cell to the ion distribution in the vicinity of these hotspots. The connection is made via an order-of-magnitude result that defines the Li ion adsorption onto the anode during charging

$$\frac{-i}{\text{Pe}^{1/3} D c_{\text{bulk}}/\delta} = \frac{3^{1/3}(1-\epsilon)}{\Gamma(1/3)} \left(\frac{x}{\delta}\right)^{-1/3} + \epsilon \frac{\sqrt{\pi}(3/2)^{1/3}}{\Gamma(1/6)} (k\delta)^{1/3} \left(\sin(kx) - \sqrt{3}\cos(kx)\right) + \mathcal{O}[\epsilon] \tag{1}$$

The SAW-driven mechanism reducing dendrite growth and facilitating dense Li plating is counterintuitive. Acoustic streaming driven by SAW causes fluid flow in the interelectrode gap. During charging, the Li$^+$ ion flux is generally enhanced by the flow as indicated by the first of the two terms on the right-hand side of Equation (1). However, this spatially ($x^{-1/3}$) decaying ion flux is perturbed by the second term on the right-hand side of Equation (1), which represents the variation in ion flux due to the presence of localized hotspots that arise from the initial electrode roughness. The combined contribution of both terms indicates the key to eliminating the possibility of dendrite growth: the dominance of the first term over the second. We seek the critical length, x_{crit}, over which the spatially oscillatory behavior of the second term is suppressed by requiring the change in ion absorption current, i, with respect to x, d($-i$)/d$x > 0$. This avoids a sign change in the current and localized regions of enhanced ion flux—hotspots that will lead

ADVANCED
SCIENCE NEWS

www.advancedsciencenews.com

ADVANCED
MATERIALS

www.advmat.de

to dendrites and porous deposition. With some effort, the critical length $x_{crit} \approx \lambda \sqrt{Pe}/18$.

The effect of the flow via the Peclet number Pe is to produce a region of size x_{crit} over which nonuniform ion deposition is prevented. The size of this region depends upon the wavelength of the initial roughness, $\lambda = 200$ μm, both an artificial construct to avoid lengthy computations in favor of useful, analysis-based design tools and a fair representation of as-supplied, pristine Li surface morphology as indicated in Figure S6 (Supporting Information). The Peclet number linearly depends upon the acoustic streaming flow, and this helps us define the characteristics required from the SAW device to ensure the critical length is at least equivalent to the battery size—$L_{bat} \approx$ 10 mm in our case.

If we equate $x_{crit} \approx L_{bat}$, and substitute in the definition for the Peclet number, we may identify the necessary flow velocity required to avoid nonuniform ion deposition over a region equivalent to the size of the battery, $u_{c,crit} \approx D(18L_{bat}\lambda)/\ell \approx 0.1$ m s^{-1} in our system. This allows us to determine the SAW input power required[39] to suppress dendrites throughout, $P_{crit} = \rho \alpha w c u_{c,crit}^2 \approx 0.1$ W, where $\alpha = 455$ μm refers to the attenuation length of the SAW in the fluid-loaded LN substrate, $w \approx 10$ mm is the aperture or width of the SAW, $c = 1498$ m s^{-1} is the speed of sound in the electrolyte, and $\rho = 998$ kg m^{-3} is the electrolyte density. We may also determine the ideal frequency to use for the SAW by equating the attenuation length of the acoustic wave, β, to the battery size, $\beta = L_{bat}$. This ensures locally generated acoustic streaming throughout the battery, helping to overcome the presence of the separator and still induce fluid flow over the entire interelectrode gap. The frequency is $f_\beta = \sqrt{(\rho c_{SAW}^3)/[4\pi^3(\mu + \mu')L_{bat}]} \approx 10^8$ Hz, the reason we choose 100 MHz in this study. The speed of the Rayleigh wave SAW in the LN substrate is $c_{SAW} = 3900$ m s^{-1} and the dynamic and dilatational viscosities of the electrolyte are, respectively, $\mu = 1$ s mPa and $\mu' = 3$ s mPa. These values are consistent with our experimental observations in the ability to suppress nonuniform Li$^+$ ion deposition with SAW in prototype Li metal batteries.

We have devised a chemistry-agnostic means for avoiding ion depletion and dendrite growth in liquid electrolyte batteries. Adopting small, high-frequency ultrasound generators to drive electrolyte flow within the interelectrode gaps gives rise to ion flux distributions that render potential locations of dendrite growth stable within a specific distance from the ultrasound source. This distance is independent of the details of the flow as long as the Peclet number is sufficiently large. This is fortunately possible with the acoustic streaming induced by our ultrasound devices and make practical Li metal rechargeable batteries possible, even with rapid charge rates and the choice of electrode materials and electrolytes that would normally be considered unrealistic. The Li‖Cu configuration, as an example, was able to cycle until 6 mA cm^{-2} current density with reasonable Coulombic efficiencies above 80% throughout. Moreover, the Li‖LiFePO$_4$ configuration can deliver 95 mAh g^{-1} capacity after 200 cycles at 2 C charge and discharge rates. Dense plating of Li in both cell types was shown with SAW, and compared to the significant porosity and dendrites present in otherwise identical cells without SAW.

We anticipate a remarkable freedom in the choice of battery electrochemistry and operation to be facilitated from this simple technology, enabling greater efficiency, utility, and sustainability of rechargeable batteries for a broad swath of current and future applications.

Experimental Section

Cell and SAW Device Fabrication: Copper (10 μm thick, MTI Corporation) was immersed in 1 M HCl followed by rinsing first with water and then with acetone to remove surface impurities and oxides before use as electrodes in all experiments. The Li (250 μm thick, MTI Corporation) was carefully scraped (245 μm thick after scraping) to remove any oxide layers before use as electrodes in all experiments. The lithium iron phosphate (LFP) electrode was prepared by first mixing LFP powder (MTI Corporation), polyvinylidene fluoride (PVDF) (Sigma Aldrich), and carbon black (C-preme LLC) in the mass ratio of LFP:PVDF:C = 75%:10%:15%; then made into a slurry by mixing with *N*-methyl-2-pyrrolidone (Sigma-Aldrich) as a solvent; pour-cast on Al foil; and finally dried in a vacuum oven for 12 h. The areal capacity is around 1 mAh cm^{-2}. Commercial grade 1 M solution of lithium hexafluorophosphate (LiPF$_6$) in a 1:1 (w/w) mixture of ethylene carbonate (EC) and diethyl carbonate (DEC) (BASF) was used as the electrolyte. Finally, a Celgard 480 separator was used between the cathode and anode.

The SAW device was fabricated through lift-off lithography to deposit 28 pairs of unweighted Au/Cr fingers and form an optimal[14] interdigital transducer (IDT) onto a 500 μm thick 127.68° Y-rotated, X-propagating cut lithium niobate substrate (LiNbO$_3$ (LN), Roditi).[17,18] The SAW device was then coated with parylene C[40] using chemical vapor deposition (PDS 2010 parylene coater system, Specialty Coating Systems) to prevent reactions with the electrolyte (see Supporting Information). The baseline LMB and SAW-integrated LMB were assembled inside an argon-filled glovebox (MTI Corporation), where the moisture level and O$_2$ level were both <1 ppm. Both the baseline and SAW LMB cells were formed from perfluoroalkoxy alkane nuts, back and front ferrules, and main housings (PFA-820-6, Swagelock) in conjunction with current collectors (304 stainless steel rods, McMaster-Carr Supply Corporation), as illustrated in Figure S2 (Supporting Information), to both seal the electrolyte and electrode from exposure to air and to safely test the cells.

Electrochemical Measurement: Electrochemical studies were carried out in the Swagelock-based cell, placing the SAW device on one side within the housing and perpendicular to the electrode gap as shown in Figure S2 (Supporting Information). The Coulombic efficiency measurements during Li plating and stripping were performed on Li‖Cu cells, where Cu serves as the working electrode and Li foil serves as the counter electrode. The Li was deposited on Cu at various current densities with a capacity of 1 mAh cm^{-2}. The deposited Li was then fully stripped to a cutoff voltage of 1 V. The Coulombic efficiency was defined as the amount of stripped Li divided by the amount of plated Li, and the average Coloumbic efficiency was calculated from this result for a range of current densities; the error bars denote the minimum and maximum measured values.

LiFePO$_4$ was used as the cathode while Li metal served as the counter electrode in full cells tested using standard galvanostatics. The charge and discharge currents were calculated based on the electrode size. For the baseline cell, the SAW device was present but was left off throughout testing. For the SAW-driven cell, the SAW device was turned on upon detection of the charging of the cell and was turned off during discharge. The charge–discharge cycling and the associated operation of the SAW device were automated during the experiments (LabVIEW), with a signal generator (SG-380, Stanford Research Systems) and amplifier (ZHL-1-2W, Mini-Circuits) used to drive the SAW device.

Morphological Characterization: The cycled batteries were disassembled inside an argon-filled glovebox, the electrodes were collected, and the electrode samples were rinsed with dimethyl carbonate (Sigma-Aldrich)

to remove the residual electrolyte on the surface of the electrode. The samples were then attached to a specimen holder (Ted Pella) using double-side carbon tape (Ted Pella) and sealed within an aluminized polyethylene bag inside the glovebox for transferring samples to the SEM. After transport to the SEM, the samples were quickly transferred from the bag to the scanning electron microscopy vacuum chamber (SEM Quanta 250, FEI Corp.) for imaging at 5 kV. The samples were exposed to air for less than three seconds.

Supporting Information

Supporting Information is available from the Wiley Online Library or from the author.

Conflict of Interest

The authors declare no conflict of interest.

Author Contributions

J.F. conceived the idea and supervised the research. A.H. devised and conducted laboratory embodiments to demonstrate its utility and basic principles. H.L. improved the laboratory experiments to obtain better cycling data and directly supervised A.H.'s Li‖Cu cell testing work. O.M. devised, conducted, and wrote the closed-form analysis of the Li$^+$ ion deposition phenomena. A.H. devised and performed the computational analysis of the SAW-driven flow and Li$^+$ ion deposition phenomena P.L. supervised H.L. throughout, supervised the advanced battery testing results and interpretation of those results. A.H. wrote the initial and subsequent paper drafts, and produced all experimental data reported within. J.F. heavily revised the paper, and all authors subsequently made final revisions to the paper.

[1] J. Liu, Z. Bao, Y. Cui, E. J. Dufek, J. B. Goodenough, P. Khalifah, Q. Li, B. Y. Liaw, P. Liu, A. Manthiram, *Nat. Energy* **2019**, *4*, 180.

[2] R. Schmuch, R. Wagner, G. Hörpel, T. Placke, M. Winter, *Nat. Energy* **2018**, *3*, 267.

[3] J. Betz, G. Bieker, P. Meister, T. Placke, M. Winter, R. Schmuch, *Adv. Energy Mater.* **2019**, *9*, 1803170.

[4] G. W. Zheng, T. Wei, *Nat. Energy* **2017**, *2*, 17029.

[5] S. Goriparti, E. Miele, F. De Angelis, E. Di Fabrizio, R. P. Zaccaria, C. Capiglia, *J. Power Sources* **2014**, *257*, 421.

[6] X. B. Cheng, R. Zhang, C. Z. Zhao, Q. Zhang, *Chem. Rev.* **2017**, *117*, 10403.

[7] M. J. Zachman, Z. Tu, S. Choudhury, L. A. Archer, L. F. Kourkoutis, *Nature* **2018**, *560*, 345.

[8] P. Albertus, S. Babinec, S. Litzelman, A. Newman, *Nat. Energy* **2018**, *3*, 16.

[9] J. Tarascon, M. Armand, *Nature* **2001**, *414*, 359.

[10] Z. Lu, Q. Liang, B. Wang, Y. Tao, Y. Zhao, W. Lv, D. Liu, C. Zhang, Z. Weng, J. Liang, H. Li, Q.-H. Yang, *Adv. Energy Mater.* **2019**, *9*, 1803186.

[11] K. Shen, Z. Wang, X. Bi, Y. Ying, D. Zhang, C. Jin, G. Hou, H. Cao, L. Wu, G. Zheng, Y. Tang, X. Tao, J. Lu, *Adv. Energy Mater.* **2019**, 1900260.

[12] H. Lai, *US 6,159,853*, **2000**.

[13] Y. Lin, *CN 201,210,444,599*, **2014**.

[14] W. Connacher, N. Zhang, A. Huang, J. Mei, S. Zhang, T. Gopesh, J. Friend, *Lab Chip* **2018**, *18*, 1952.

[15] H. Li, J. R. Friend, L. Y. Yeo, *Biomed. Microdevices* **2007**, *9*, 647.

[16] R. Shilton, M. K. Tan, L. Y. Yeo, J. R. Friend, *J. Appl. Phys.* **2008**, *104*, 014910.

[17] A. Huang, M. Miansari, J. Friend, *Appl. Phys. Lett.* **2018**, *113*, 034103.

[18] J. Friend, L. Y. Yeo, *Rev. Mod. Phys.* **2011**, *83*, 647.

[19] C. Campbell, *Surface Acoustic Wave Devices for Mobile and Wireless Communications*, Academic Press, Inc., San Diego, CA, USA **1998**.

[20] X. Q. Zhang, X. B. Cheng, X. Chen, C. Yan, Q. Zhang, *Adv. Funct. Mater.* **2017**, *27*, 1605989.

[21] C. Yan, X.-B. Cheng, Y. Tian, X. Chen, X.-Q. Zhang, W.-J. Li, J.-Q. Huang, Q. Zhang, *Adv. Mater.* **2018**, *30*, 1707629.

[22] J. Zheng, M. H. Engelhard, D. Mei, S. Jiao, B. J. Polzin, J.-G. Zhang, W. Xu, *Nat. Energy* **2017**, *2*, 17012.

[23] Y. Liu, D. Lin, Z. Liang, J. Zhao, K. Yan, Y. Cui, *Nat. Commun.* **2016**, *7*, 10992.

[24] K. Yan, Z. Lu, H.-W. Lee, F. Xiong, P.-C. Hsu, Y. Li, J. Zhao, S. Chu, Y. Cui, *Nat. Energy* **2016**, *1*, 16010.

[25] H. Liu, X. Yue, X. Xing, Q. Yan, J. Huang, V. Petrova, H. Zhou, P. Liu, *Energy Storage Mater.* **2019**, *16*, 505.

[26] C. Fang, J. Li, M. Zhang, Y. Zhang, F. Yang, J. Z. Lee, M.-H. Lee, J. Alvarado, M. A. Schroeder, Y. Yang, B. Lu, N. Williams, M. Ceja, L. Yang, M. Cai, J. Gu, K. Xu, X. Wang, Y. S. Meng, *Nature* **2019**, *572*, 511.

[27] X. Wang, W. Zeng, L. Hong, W. Xu, H. Yang, F. Wang, H. Duan, M. Tang, H. Jiang, *Nat. Energy* **2018**, *3*, 227.

[28] C. Fang, X. Wang, Y. S. Meng, *Trends Chem.* **2019**, *1*, 152.

[29] G. Li, Z. Liu, D. Wang, X. He, S. Liu, Y. Gao, A. AlZahrani, S. H. Kim, L.-Q. Chen, D. Wang, *Adv. Energy Mater.* **2019**, *9*, 1900704.

[30] L. O. Valoen, J. N. Reimers, *J. Electrochem. Soc.* **2005**, *152*, A882.

[31] J. Diggle, A. Despic, J. Bockris, *J. Electrochem. Soc.* **1969**, *116*, 1503.

[32] R. Akolkar, *J. Power Sources* **2013**, *232*, 23.

[33] W. Thielicke, E. Stamhuis, *J. Open Res. Software* **2014**, *2*, e30.

[34] C. Monroe, J. Newman, *J. Electrochem. Soc.* **2003**, *150*, A1377.

[35] D. M. Tartakovsky, D. Xiu, *J. Comput. Phys.* **2006**, *217*, 248.

[36] J. Jorne, Y. J. Lii, K. E. Yee, *J. Electrochem. Soc.* **1987**, *134*, 1399.

[37] A. Ehrl, J. Landesfeind, W. A. Wall, H. A. Gasteiger, *J. Electrochem. Soc.* **2017**, *164*, A826.

[38] W. Zhang, H. A. Stone, J. Sherwood, *J. Phys. Chem.* **1996**, *100*, 9462.

[39] M. B. Dentry, L. Y. Yeo, J. R. Friend, *Phys. Rev. E* **2014**, *89*, 013203.

[40] K. Länge, S. Grimm, M. Rapp, *Sens. Actuators, B* **2007**, *125*, 441.